

Imaging the electron charge density in monolayer MoS₂ at the Ångstrom scale

Joel Martis^{1*}, Sandhya Susarla^{2,3,4*}, Archith Rayabharam⁵, Cong Su^{6,10,11}, Timothy Paule^{6,10,11}, Philipp Pelz^{2,7}, Cassandra Huff⁸, Xintong Xu¹, Hao-Kun Li¹, Marc Jaikissoon⁸, Victoria Chen⁸, Eric Pop⁸, Krishna Saraswat⁸, Alex Zettl^{6,10,11}, Narayana R. Aluru⁹, Ramamoorthy Ramesh^{6,10}, Peter Ercius^{2†}, Arun Majumdar^{1‡}

¹*Department of Mechanical Engineering, Stanford University*

²*The National Center for Electron Microscopy (NCEM), The Molecular Foundry, Lawrence Berkeley National Laboratory*

³*Materials Science Division, Lawrence Berkeley National Laboratory*

⁴*School for Engineering of Matter, Transport and Energy, Arizona State University*

⁵*Department of Mechanical Engineering, University of Illinois Urbana-Champaign*

⁶*Department of Physics, University of California Berkeley*

⁷*Institute of Micro- and Nanostructure Research & Center for Nanoanalysis and Electron Microscopy (CENEM), Department of Materials Science, Friedrich-Alexander-Universität Erlangen-Nürnberg (FAU), Erlangen, Germany*

⁸*Department of Electrical Engineering, Stanford University*

⁹*Department of Mechanical Engineering, The University of Texas at Austin*

¹⁰*Department of Materials Science and Engineering, University of California Berkeley*

¹¹*Kavli Energy NanoScience Institute, University of California Berkeley*

* These authors contributed equally to this work

† corresponding author (email: percius@lbl.gov)

‡ corresponding author (email: amajumdar@stanford.edu)

Abstract: Four-dimensional scanning transmission electron microscopy (4D-STEM) has recently gained widespread attention for its ability to image atomic electric fields with sub-Ångstrom spatial resolution. These electric field maps represent the integrated effect of the nucleus, core electrons and valence electrons, and separating their contributions is non-trivial. In this paper, we utilized simultaneously acquired 4D-STEM center of mass (CoM) images and annular dark field (ADF) images to determine the electron charge density in monolayer MoS₂. We find that both the core electrons and the valence electrons contribute to the derived electron charge density. However, due to blurring by the probe shape, the valence electron contribution forms a nearly featureless background while most of the spatial modulation comes from the core electrons. Our findings highlight the importance of probe shape in interpreting charge densities derived from 4D STEM.

Introduction

Four-dimensional scanning transmission electron microscopy (4D-STEM) has become a versatile tool in recent years with various applications¹. One technique measures electric fields by calculating the center of mass (CoM) of the central spot in the diffraction pattern acquired at each electron probe position and has been shown to reveal atomic electric fields². With the help of aberration-corrected STEMs and fast pixelated detectors^{3–6}, sub-Angstrom electric field and charge density mapping using 4D-STEM CoM imaging has become feasible with numerous studies in literature^{7–12}. This is an important development, because atomic electric fields emerge from a combination of nuclear effects along with the electrons that form chemical bonds around them. The ability to map valence electrons with sub-Ångstrom resolution can potentially lead to new insights about chemical bonding, charge transfer effects, polarization, ferroelectricity, ion transport, and much more^{13,14}.

Other techniques are limited in their ability to directly image the electron charge density. Annular dark field (ADF) STEM, for example, images atom positions based on the high-angle scattering of incident electrons by the nucleus^{15,16}. Electron energy loss spectroscopy (EELS) can identify core electron states at atomic resolution¹⁷ but cannot measure their charge density directly. Valence EELS (VEELS) is limited by the delocalization of the excitation on the nanometer scale, much larger than the sizes of the valence orbitals themselves¹⁸. Although recent VEELS work has shown atomic-scale contrast in certain energy ranges in graphene, the contrast is a function of inelastic scattering cross sections between different orbitals making it is non-trivial to isolate valence electron charge densities¹⁹. Valence electron densities are commonly measured using scanning tunneling microscopy (STM)²⁰, but these are limited to surfaces and energy ranges typically a few eV below the Fermi level²¹. While previous efforts have indicated

that electron contributions are important in 4D-STEM images^{7,11}, the electron charge density hasn't been explicitly imaged so far.

In this paper, we investigate the different contributions to atomic electric fields and charge densities derived using 4D-STEM. In particular, we show how the ADF-STEM intensity channel can be used to subtract the nuclear contribution from the total charge density derived from 4D-STEM and derive the electron charge density in monolayer MoS₂. Our experimental results show good agreement with the electron charge densities predicted by density functional theory (DFT). We discuss how both core electrons and valence electrons contribute to the derived electron charge density, and how probe convolution (i.e., blurring by the probe intensity distribution) results in core electrons dominating the measured electron charge density map. Our findings point towards a need for smaller electron probes that could potentially distinguish between valence and core electrons based on orbital size.

Results

4D STEM of monolayer MoS₂. A 4D STEM dataset is acquired by scanning a focused electron probe across a sample and using a pixelated detector to image the scattered electron beam at each probe position (Fig. 1). It has been shown using Ehrenfest's theorem that the CoM of the scattered electron beam at each probe position is directly proportional to the projected electric field at that probe position, convolved with the probe intensity². Therefore, one can derive a 2D electric field map of a sample by simply computing the CoM of the scattered electron beam at every probe position as it scans across a sample. This electric field map can then be converted into a projected charge density image and an electrostatic potential image of the sample using Gauss' law.

Here, we derive atomic electric field maps of monolayer MoS₂ using 4D STEM CoM imaging. A monolayer of MoS₂ is a two-dimensional direct bandgap semiconductor in its 2H phase where the Mo atoms are sandwiched between two S atoms (Fig. 1a). The semiconducting nature and direct band gap are useful for optoelectronics and catalysis applications^{17,18}. MoS₂ therefore provides an excellent model system for our experiments. Figure 1b shows an ADF-STEM image of a unit cell of MoS₂. Simultaneously, the transmitted beam intensity is imaged using a high speed 4D-STEM camera³, and the CoM of the diffraction pattern at each probe position is computed, leading to Fig. 1c and 1d. The camera is a direct electron detector and allows for high quantum efficiency data collection at high speeds, which is critical when imaging beam sensitive materials such as monolayer MoS₂. Figures 1b-d represent unit cell averages over about 100 unit cells from a larger scan area which significantly improves the signal-to-noise ratio (see Supplementary Figure 3).

Since the CoM of the electron beam is proportional to the projected electric field at the sample, the experimental projected electric field map in Fig. 2a is derived by simply multiplying the CoM images with appropriate physical constants, following reference². The intensity of the image represents the magnitude of the electric field, and the arrows represent its direction. We observe that the centers of lattice sites, midpoints between neighboring atoms, and the center of the unit cell show zero electric field in agreement with previously reported works^{10,12}. Using the projected electric field, we computed the projected potential by integrating the field (Fig. 2b) and projected charge density using Gauss' Law (Fig. 2c). The projected charge density (Fig. 2c) is the sum of the nuclear and electron charge densities convolved with the probe intensity. The lattice sites have a net positive charge (red) because of a higher contribution from the nucleus, whereas the regions around lattice sites have a net negative charge (blue) indicating a higher

contribution from the electrons. There is also a slight asymmetry in the charge density around the center of the unit cell. It is non-trivial to separate the contributions of the nucleus and the electrons to the net charge density and the contributions of valence and core electrons to the electronic part of the net charge density.

Effect of probe convolution. The incident electron probe's shape is an Airy function with a central peak of $\sim 1\text{\AA}$ in size and so-called probe tails that extend farther beyond the central peak²². Thus, probe convolution plays a fundamental role in interpreting Figures 2a-c. Moreover, residual aberrations due to corrector alignment drift and measurement error play a significant role in determining its extended shape²³. We simulate the 4D STEM data by convolving the electric field, potential and charge density derived from DFT with the electron probe intensity calculated for 80 kV and 30 mrad convergence semi-angle along with some residual aberrations (defocus, 3-fold astigmatism, 3rd order spherical aberration, 4-fold astigmatism) and 1.1 \AA Gaussian blurring to account for source size and other blurring factors (Figures 2d-f). These aberrations were determined empirically to match experimental data and are within reasonable limits of microscope performance during extended operation. The contributions to the charge density image arising from different aberrations is illustrated in Fig. 3, where the top row shows the probe shape, and the bottom row shows the corresponding probe convolved charge density image. An ideal diffraction limited probe at 30 mrad gives rise to a charge density image that is about 4 times higher in magnitude compared to our experimental data (Fig. 3a1, b1). When 3nm defocus (denoted as C_{10} following Krivanek's notation²⁴) and 10 μm 3rd order spherical aberration (C_{30}) are added, the probe tails are slightly extended resulting in a decrease in peak intensities (Fig. 3a2, b2). When 200 nm 3-fold astigmatism (C_{23}) is introduced, the probe tails are greatly extended, resulting in diminished charge density values (Fig. 3a3,b3). Rotating the

probe also changes the apparent negative charge distribution in the unit cell (Fig. 3a4,b4).

Finally, adding 5 μm 4-fold astigmatism (C_{23}) gives rise to an asymmetry similar to that observed in experiment. Other combinations of aberrations may lead to similar results; however, our analysis helps explain two important issues. (1) The charge density image intensities observed in experiments (ours and others^{12,25,10}) are lower than predicted by ideal simulations likely because of intensity redistribution in the probe tails due to residual aberrations. (2) The origin of asymmetry in the experimental charge density is due to the shape and orientation of the probe. Importantly, residual aberrations are difficult to quantify fully since they may not directly affect the point resolution of the image which is largely determined by the full width half maximum of the probe's central peak. However, they can have an outsized impact on the extended intensity distribution in the charge density image and must be taken into account before making any conclusions about the actual distribution of electrons around atoms.

To understand the effect of probe convolution on the electron charge density, we convolve the DFT-derived electron charge density with the simulated probe shape as determined earlier (Fig 4). Fig 4a and 4b show the DFT simulated valence and core electron charge densities for a hexagonal unit cell of MoS_2 . The valence electrons consist of the $3s^2 3p^4$ electrons from S and the $4d^5 6s^1$ from Mo. We observe that the valence electrons are predominantly concentrated on the S atom because of its higher electronegativity. The core electron charge density shows a higher charge density on Mo as expected. Probe convolution (Figures 4c and 4d) shows that the core electron charge density is now delocalized on the order of 1 \AA and the valence electron charge density is nearly featureless. Their sum, Fig 4e, produces the net electron charge density where we observe that the spatial variation in charge density mostly comes from the core electrons, with the valence electrons contributing as a uniform background of about -2 e/\AA^2 .

Imaging the electron charge density. To isolate the electron charge density experimentally, we subtract the nuclear charge density determined using the ADF-STEM image from the total charge density derived using 4D STEM CoM imaging. Because the nucleus, which is confined to a few femtometres in size, scatters electrons to much higher angles relative to core electrons (0.1 Å) and valence electrons (1 Å), it predominantly contributes to ADF-STEM image contrast. Furthermore, because the nuclear scattering is proportional to Z^x , where Z is the atomic number and x ranges from 1.5-2 depending on the collection geometry, image deconvolution and the Z of the studied elements^{15,26}, a nuclear charge image can be quantitatively derived from the ADF-STEM. In our experiments, we find that the ADF-STEM intensity for S and Mo scales as $\sim Z^{1.9}$ (see Supplementary Note 1 and Supplementary Figure 5). Using this, we assign each atom a discrete nuclear charge. Ideally, one could calibrate a given ADF-STEM detector with several types of atoms and derive a direct correlation between observed ADF-STEM intensity and quantitative nuclear charge, as done in¹⁵. This could allow for direct quantification of the nuclear charge of atomic columns of unknown composition and thickness. Once a nuclear charge is assigned as a delta function, we convolve it with the probe intensity along with 1.1 Å Gaussian blurring (see Supplementary Figure 5). Fig. 5b shows the nuclear charge density image convolved with the probe intensity, which when subtracted from the net charge in Fig. 5(a), gives the electron charge density in Fig. 5(c). Fig. 5d shows the line profiles comparing the experimentally derived and simulated electron charge densities. We observe that the spatial modulation in the experimental electron charge density comes from the core electrons, with the valence electrons contributing as a uniform background. This means that even though CoM imaging can image electron distributions, probe convolution blurs the valence electron density forming an almost uniform, unmodulated background of about $-2 \text{ e}/\text{\AA}^2$. We note that the

experimental noise (std $\sigma \sim 0.2\text{e}/\text{\AA}^2$) is much lower than valence electron density, indicating that we can indeed measure the effect of the valence electron charge density.

Discussion

We have imaged the electron charge density in monolayer MoS₂ using 4D STEM CoM imaging and explored the contributions from the valence v/s core electrons. We found that probe convolution smooths out any features in the valence electron charge density, and the spatial modulation in the derived electron charge density mostly comes from core electrons. Our findings highlight the importance of probe shape in quantitatively interpreting CoM-derived charge density images. Residual aberrations that extend probe tails can significantly diminish image intensities, and asymmetry in the probe shape can give rise to asymmetric charge densities. Residual aberrations in the probe must be accounted for when interpreting the spatial distribution of charge densities in CoM 4D-STEM results.

Because valence electron orbitals are of interest for understanding the chemical and electronic properties of materials, an important question to address is – can the valence electron orbitals be imaged? In order to separate valence and core electron charge densities, one needs an electron probe size that is much smaller than the 1 Å feature size of valence electron orbitals. Achieving this experimentally is currently challenging as state-of-the-art probes are on the order of valence electron orbital sizes (about 0.7 Å at 80 keV and 0.5 Å at 300 keV). Post-processing reconstruction methods such as ptychography offer an indirect route to attaining super-resolution images by iteratively refining and disentangling nuisance parameters such as position errors and partial coherence^{27–30}. Spatial resolution in electron microscopy at the atomic scale is typically quantified by two approaches. Self-consistency measures like Fourier Ring correlation (FRC)³¹

or spectral signal-to-noise ratio (SSNR)³² measure the consistency of a reconstruction from two experimental datasets. If single atoms or atomic columns are visible, optical resolution can be measured by the minimum resolvable separation between atoms²⁹. Since the contribution of valence electrons to the charge density is roughly two orders of magnitude lower than the contribution of core electrons, it will be critical to evaluate the sensitivity of these existing resolution metrics regarding quantitative reconstruction. We emphasize here that although CoM imaging is affected by probe shape it offers a more direct route to imaging charge densities, as it simply relies on calculating the divergence of the center of mass of the scattered electron beam. Our findings point towards the need for smaller electron probes which could potentially resolve valence electron charge densities in materials.

Methods

Sample preparation. The monolayer MoS₂ is grown by the halide-assisted chemical vapor deposition method with Mo source provided by a liquid precursor. The detailed procedure is described in³³. We subsequently transfer the monolayer MoS₂ samples to a Quantifoil TEM grid (2/2, copper grid) by the standard wet transfer method using PMMA which is also described in³³. The PMMA is cleaned by acetone vapor before imaging in STEM. Optical images of MoS₂ on before and after transfer are shown in Supplementary Figure 1.

4D STEM experiments. The 4D-STEM data was acquired using a Titan 80-300 called the TEAM 0.5 at the National Center for Electron Microscopy facility of the Molecular Foundry. The machine was operated in STEM mode at 80 kV with a convergence semi-angle of 30 mrad and approximately 20 pA beam current. A direct electron detector called the 4D Camera was used to capture a diffraction pattern at each probe position. The camera has 576x576 pixels and

operates at a frate rate of 87,000 Hz. The full data set was acquired in a scan of 512x512 probe locations and 4 frames were summed at each position (Supplementary Figure 2).

Unit cell (class) averaging was carried out on the raw data to improve the SNR ratio (Supplementary Figure 3). This was done using three steps: (1) Atom positions were identified in the electrostatic potential image (since it was the less noisy compared to ADF and CoM images) using AtomSegNet³⁴, a deep learning based localization algorithm. (2) Atoms were classified into Mo and S based on the ADF image intensity. (3) Using atom positions and classes, class averaging was carried out at each atom site in the CoM, phase and charge density images to yield unit cell averaged images. We observed a significant improvement in SNR of the CoM and charge density images after averaging.

DFT Simulations. To simulate the ground state charge density distribution of the 2H-phase of MoS₂, a self-consistent analysis of the Density Functional Theory (DFT)³⁵ was performed using the Vienna Ab initio simulation (VASP)^{36,37} package. The Perdew-Burke-Ernzerhof (PBE)³⁸ exchange-correlation functional, which comes under the Generalized Gradient Approximation (GGA), was used and projected augmented wave (PAW) pseudopotentials with a 500 eV energy cutoff and Gamma-point-centered k-point of $8 \times 8 \times 2$ were used. The convergence with respect to the grid-size and cut-off energy is shown in Supplementary Figure 4 for a sample simulation. The unit cell of MoS₂ used consists of 12 atoms, with the simulation box having the dimensions $6.325 \times 5.478 \times 12.302 \text{ \AA}^3$. Before the self-consistent calculation for evaluating the charge density distribution are done, the 2H-phase of MoS₂ is relaxed using an energy convergence criteria of 10⁻⁸ eV.

STEM simulations. STEM probe intensities were calculated using methods outlined in ²². A 30 mrad aperture was used along with residual aberrations mentioned in the manuscript. 4D STEM

CoM charge densities and electric fields were simulated by convolving the simulated probe intensity with the DFT simulated electron charge density and manually added delta functions to represent nuclear charge densities. The nuclear charge image in Figure 5 was determined from the experimental ADF-STEM image. The details are described in Supplementary Note 1 and Supplementary Figure 5. All STEM calculations were performed using in-house python code.

References

1. Ophus, C. Four-Dimensional Scanning Transmission Electron Microscopy (4D-STEM): From Scanning Nanodiffraction to Ptychography and Beyond. *Microscopy and Microanalysis* Preprint at <https://doi.org/10.1017/S1431927619000497> (2019).
2. Müller, K. *et al.* Atomic electric fields revealed by a quantum mechanical approach to electron picodiffraction. *Nature Communications* **5**, (2014).
3. Ercius, P. *et al.* The 4D Camera – An 87 kHz Frame-rate Detector for Counted 4D-STEM Experiments. *Microscopy and Microanalysis* **26**, (2020).
4. Haas, B. *et al.* High-Fidelity 4D-STEM Enabled by Live Processing at 15'000 Detector Frames Per Second. *Microscopy and Microanalysis* **27**, (2021).
5. Jannis, D. *et al.* Event driven 4D STEM acquisition with a Timepix3 detector: Microsecond dwell time and faster scans for high precision and low dose applications. *Ultramicroscopy* **233**, (2022).
6. Philipp, H. T. *et al.* Very-High Dynamic Range, 10,000 Frames/Second Pixel Array Detector for Electron Microscopy. *Microscopy and Microanalysis* **28**, (2022).

7. Zheng, Q. *et al.* Direct visualization of anionic electrons in an electride reveals inhomogeneities. *Science Advances* **7**, (2021).
8. Shibata, N. *et al.* Electric field imaging of single atoms. *Nature Communications* **8**, (2017).
9. Hachtel, J. A., Idrobo, J. C. & Chi, M. Sub-Ångstrom electric field measurements on a universal detector in a scanning transmission electron microscope. *Advanced Structural and Chemical Imaging* **4**, (2018).
10. Müller-Caspary, K. *et al.* Atomic-scale quantification of charge densities in two-dimensional materials. *Physical Review B* **98**, (2018).
11. Gao, W. *et al.* Real-space charge-density imaging with sub-ångström resolution by four-dimensional electron microscopy. *Nature* **575**, (2019).
12. Fang, S. *et al.* Atomic electrostatic maps of 1D channels in 2D semiconductors using 4D scanning transmission electron microscopy. *Nature Communications* **10**, (2019).
13. Bredtmann, T., Ivanov, M. & Dixit, G. X-ray imaging of chemically active valence electrons during a pericyclic reaction. *Nature Communications* **5**, (2014).
14. Yamauchi, K. & Barone, P. Electronic ferroelectricity induced by charge and orbital orderings. *Journal of Physics Condensed Matter* **26**, (2014).
15. Krivanek, O. L. *et al.* Atom-by-atom structural and chemical analysis by annular dark-field electron microscopy. *Nature* **464**, (2010).

16. Nellist, P. D. & Pennycook, S. J. The principles and interpretation of annular dark-field Z-contrast imaging. *Advances in Imaging and Electron Physics* **113**, (2000).
17. Monkman, E. J. *et al.* Quantum many-body interactions in digital oxide superlattices. *Nature Materials* **11**, (2012).
18. Egerton, R. F. *Electron Energy-Loss Spectroscopy in the Electron Microscope*. *Electron Energy-Loss Spectroscopy in the Electron Microscope* (2011). doi:10.1007/978-1-4419-9583-4.
19. Kapetanakis, M. D. *et al.* Low-loss electron energy loss spectroscopy: An atomic-resolution complement to optical spectroscopies and application to graphene. *Physical Review B - Condensed Matter and Materials Physics* **92**, (2015).
20. Addou, R., Colombo, L. & Wallace, R. M. Surface Defects on Natural MoS₂. *ACS Applied Materials and Interfaces* **7**, (2015).
21. Li, X. & Zhu, H. Two-dimensional MoS₂: Properties, preparation, and applications. *Journal of Materiomics* **1**, (2015).
22. Kirkland, E. J. *Advanced Computing in Electron Microscopy*. *Advanced Computing in Electron Microscopy* (2020). doi:10.1007/978-3-030-33260-0.
23. Kirkland, E. J. On the optimum probe in aberration corrected ADF-STEM. *Ultramicroscopy* **111**, (2011).
24. Krivanek, O. L., Dellby, N. & Lupini, A. R. Towards sub-Å electron beams. in *Ultramicroscopy* vol. 78 (1999).

25. Wen, Y. *et al.* Mapping 1D Confined Electromagnetic Edge States in 2D Monolayer Semiconducting MoS₂ Using 4D-STEM. *ACS Nano* **16**, (2022).
26. Lebeau, J. M., Findlay, S. D., Allen, L. J. & Stemmer, S. Quantitative atomic resolution scanning transmission electron microscopy. *Physical Review Letters* **100**, (2008).
27. Maiden, A. M. & Rodenburg, J. M. An improved ptychographical phase retrieval algorithm for diffractive imaging. *Ultramicroscopy* **109**, (2009).
28. Chen, Z. *et al.* Mixed-state electron ptychography enables sub-angstrom resolution imaging with picometer precision at low dose. *Nature Communications* **11**, (2020).
29. Jiang, Y. *et al.* Electron ptychography of 2D materials to deep sub-ångström resolution. *Nature* **559**, (2018).
30. Chen, Z. *et al.* Electron ptychography achieves atomic-resolution limits set by lattice vibrations. *Science* (1979) **372**, (2021).
31. van Heel, M. & Schatz, M. Fourier shell correlation threshold criteria. *Journal of Structural Biology* **151**, (2005).
32. Unser, M., Trus, B. L. & Steven, A. C. A new resolution criterion based on spectral signal-to-noise ratios. *Ultramicroscopy* **23**, (1987).
33. Ji, Q. *et al.* Revealing the Brønsted-Evans-Polanyi relation in halide-activated fast MoS₂ growth toward millimeter-sized 2D crystals. *Science Advances* **7**, (2021).
34. Lin, R., Zhang, R., Wang, C., Yang, X. Q. & Xin, H. L. TEMImageNet training library and AtomSegNet deep-learning models for high-precision atom segmentation,

- localization, denoising, and deblurring of atomic-resolution images. *Scientific Reports* **11**, (2021).
35. Kohn, W. & Sham, L. J. Self-consistent equations including exchange and correlation effects. *Physical Review* **140**, (1965).
 36. Kresse, G. & Furthmüller, J. Efficiency of ab-initio total energy calculations for metals and semiconductors using a plane-wave basis set. *Computational Materials Science* **6**, (1996).
 37. Kresse, G. & Furthmüller, J. Efficient iterative schemes for ab initio total-energy calculations using a plane-wave basis set. *Physical Review B - Condensed Matter and Materials Physics* **54**, (1996).
 38. Perdew, J. P., Burke, K. & Ernzerhof, M. Generalized gradient approximation made simple. *Physical Review Letters* **77**, (1996).

Acknowledgements

JM was partly supported by the Air Force Office of Scientific Research under Grant No. FA9550-19-1-0309. JM and XX were supported as part of the Center for Enhanced Nanofluidic Transport (CENT), an Energy Frontier Research Center funded by the U.S. Department of Energy (DOE), Office of Science, Basic Energy Sciences (BES), under Award No. DE-SC0019112. The experiments were performed at the Molecular Foundry, Lawrence Berkeley National Laboratory, which is supported by the U.S. Department of Energy under contract no. DE-AC02-05CH11231. We would like to thank Gatan, Inc. as well as P Denes, A Minor, J Ciston, C Ophus, J Joseph, and Ian Johnson who contributed to the development of the 4D

Camera used in this work. This research used resources of the National Energy Research Scientific Computing Center (NERSC), a U.S. Department of Energy Office of Science User Facility located at Lawrence Berkeley National Laboratory, operated under Contract No. DE-AC02-05CH11231 using NERSC award ERCAP0020898 and ERCAP0020897. C.S., T. P., and A.Z. were supported by the Director, Office of Science, Office of Basic Energy Sciences, Materials Sciences and Engineering Division of the U.S. Department of Energy under contract no. DE-AC02-05-CH11231, within the sp²-Bonded Materials Program (KC2207) which supported materials synthesis and the van der Waals Heterostructures program (KCWF16) which supported TEM sample preparation. CH was partially supported by the National Science Foundation Graduate Research Fellowship (NSF GRFP) under Grant No. DGE-1656518, partially sponsored by the Office of Naval Research (ONR) for Hyperviper: Broadband Hyperspectral Imaging System under Award No. N00014-21-1-2788, and partially supported by University of Texas at Austin/Office of Naval Research (ONR) for the project Extraordinary Electronic Switching of Thermal Transport under Award No. UTA21-000335. VC acknowledges support from the ARCS Fellowship.

Author contributions

JM, SS and PE performed 4D STEM experiments. JM post-processed experimental data and performed STEM simulations. AR performed DFT calculations. CS, TP, MJ and VC fabricated samples. PE, PP, SS, CH, XX and HL helped with data interpretation and writing the manuscript. The work was supervised by AM, RR, AZ, PE, NA, KS and EP.

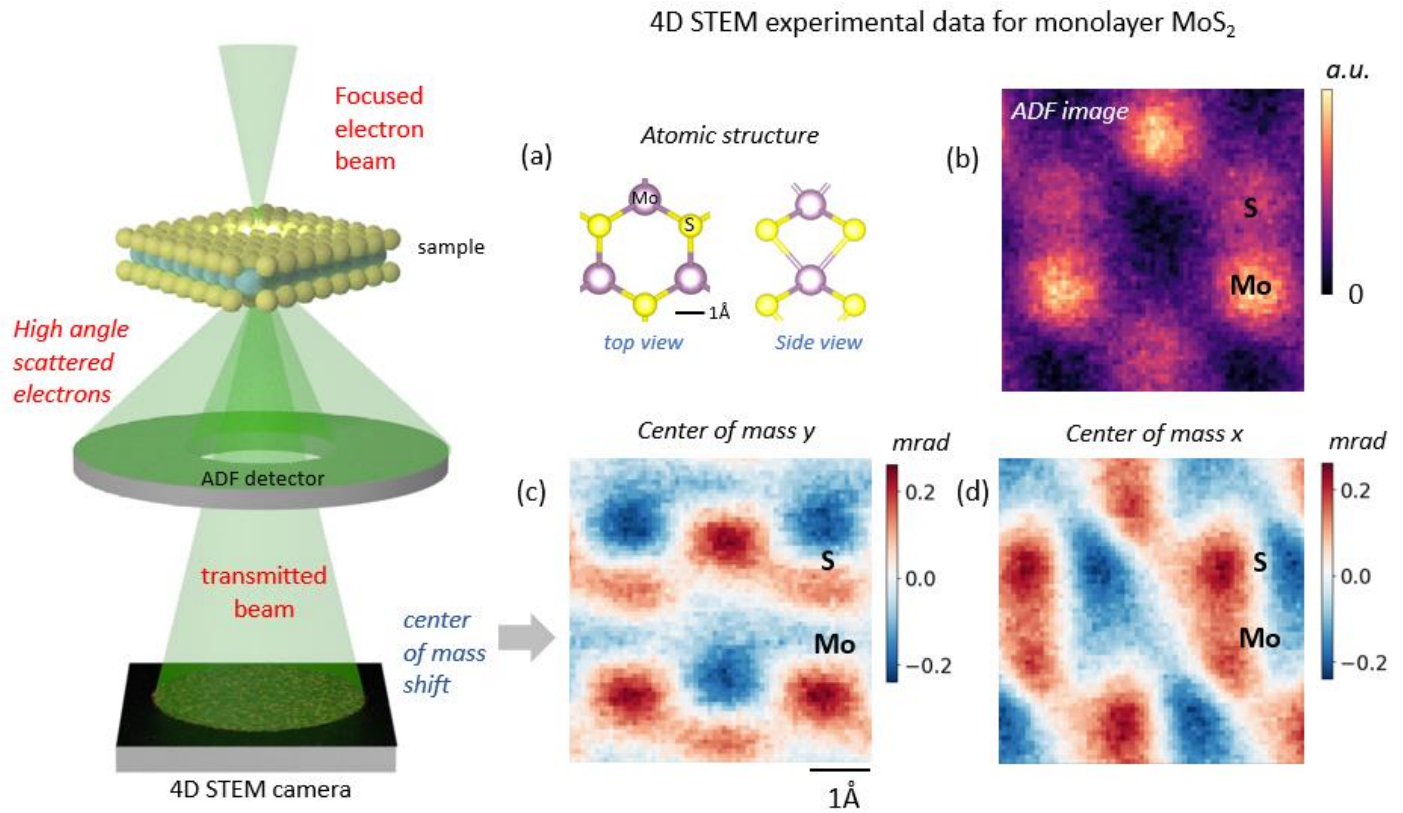


Figure 1 | 4D STEM experiments on monolayer MoS₂ (left) Schematic showing the experimental setup for simultaneous 4D STEM and ADF-STEM imaging. (a) Atomic structure of one hexagonal unit cell of MoS₂ (b) Unit cell averaged ADF-STEM image corresponding to a hexagonal unit cell (c) Center of mass along y for the unit cell and (d) center of mass along x for the unit cell

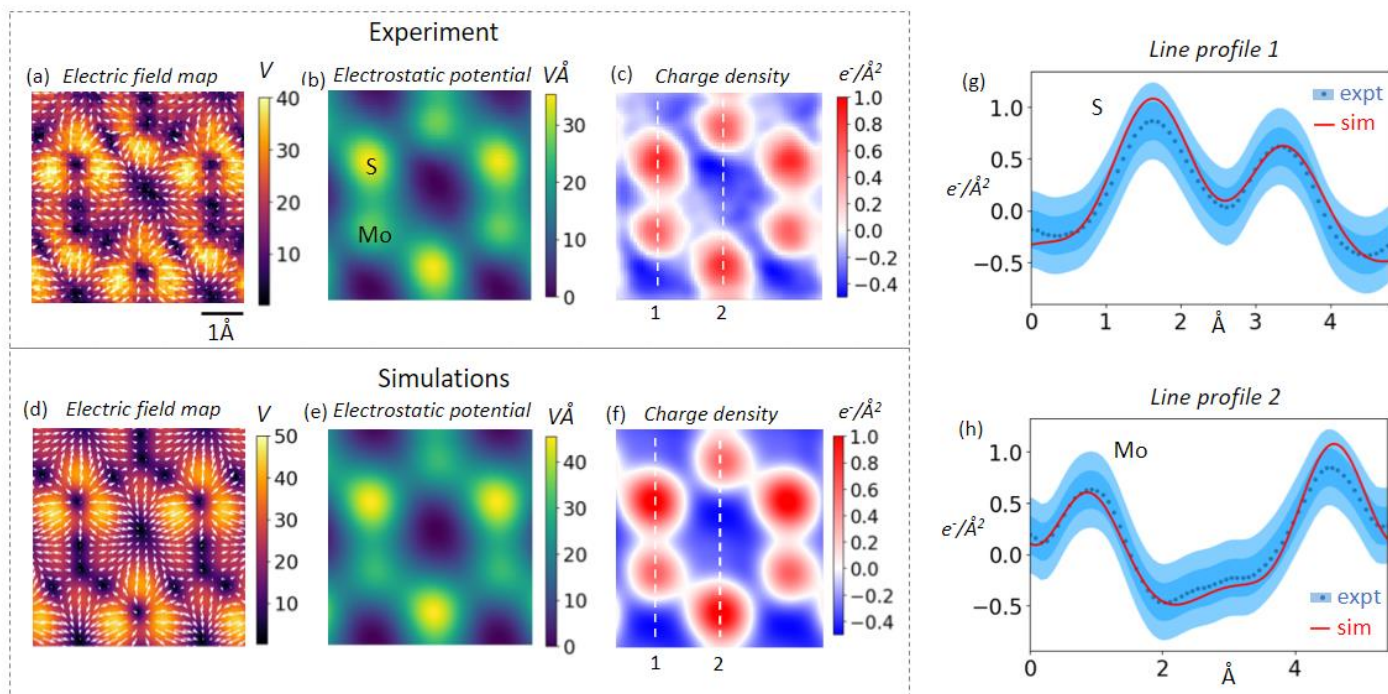


Figure 2 | Electric field and charge density maps from CoM imaging. (a) Experimental electric field map corresponding to a unit cell, the color intensity indicates the magnitude and arrows indicate the direction of the electric field (b) Electrostatic potential and (c) charge density corresponding to (a) with red indicating net positive charge and blue indicating net negative charge. Simulated (d) electric field map from DFT, (e) electrostatic potential and (f) charge density convolved with an electron probe at 80 keV and 30 mrad convergence semiangle. (g & h) Line profiles (1 & 2) of the charge density comparing experiment with simulation. The dark(light) blue shaded regions indicate one(two) standard deviation(s) on either side of the mean.

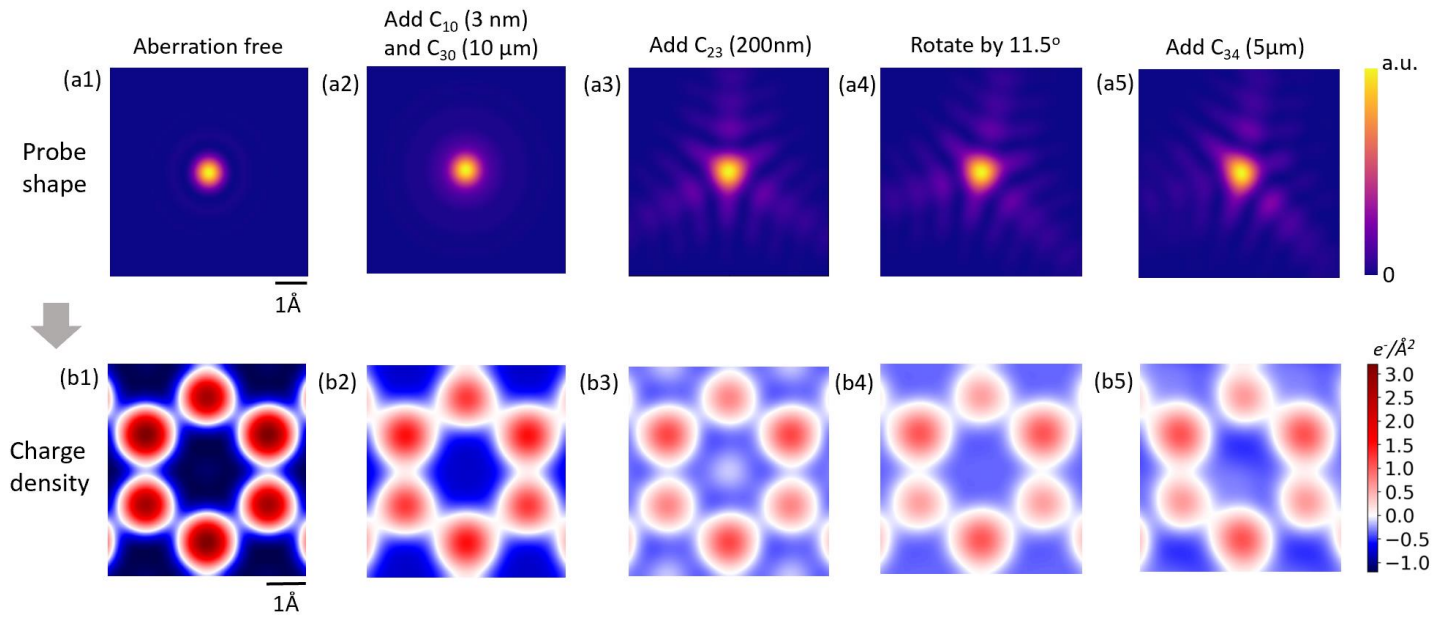


Figure 3 | Effect of probe shape and residual aberrations on the charge density image. (a1-a5) Simulated probe shapes for various conditions as stated on top of each image, with each image including the cumulative aberrations of images to its left (b1-b5) Corresponding charge density images obtained by convolving the probe intensity with DFT simulated charge densities.

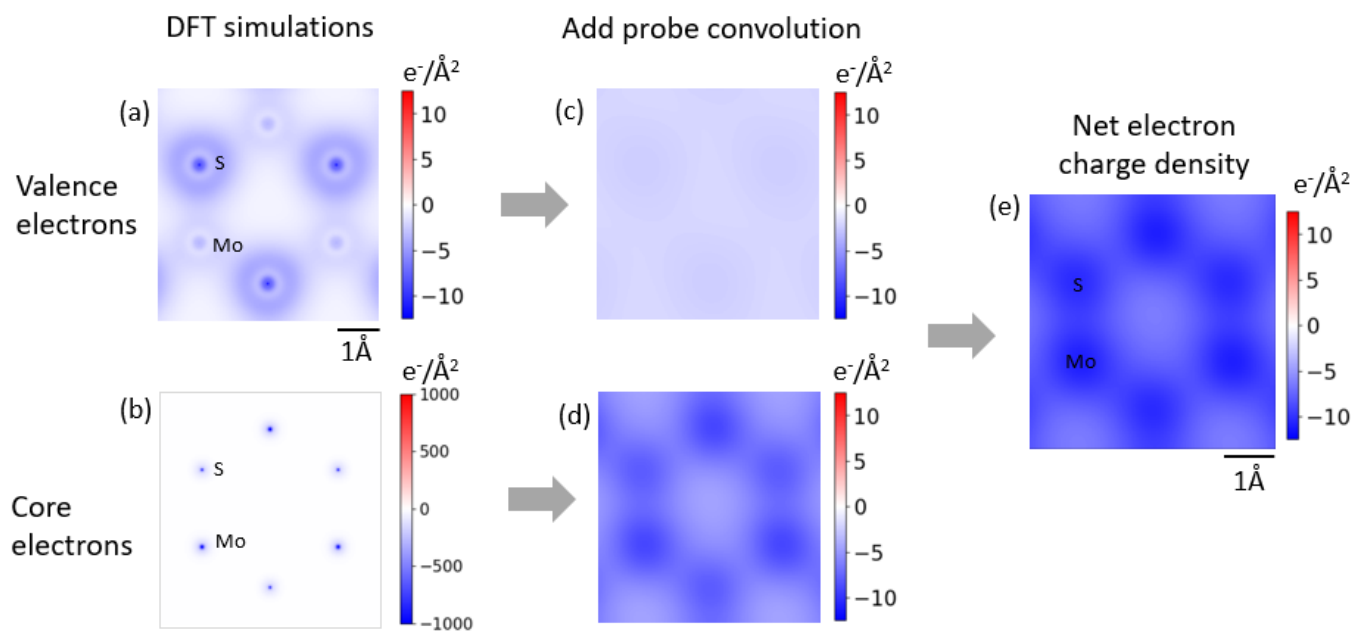


Figure 4 | Simulated contributions of valence and core electrons to the electron charge

density. DFT derived charge density showing (a) valence electrons and (b) core electrons for a hexagonal unit cell of MoS_2 . Probe convolved (c) valence and (d) core electrons. (e) Sum of (c) and (d) showing the net electron charge density

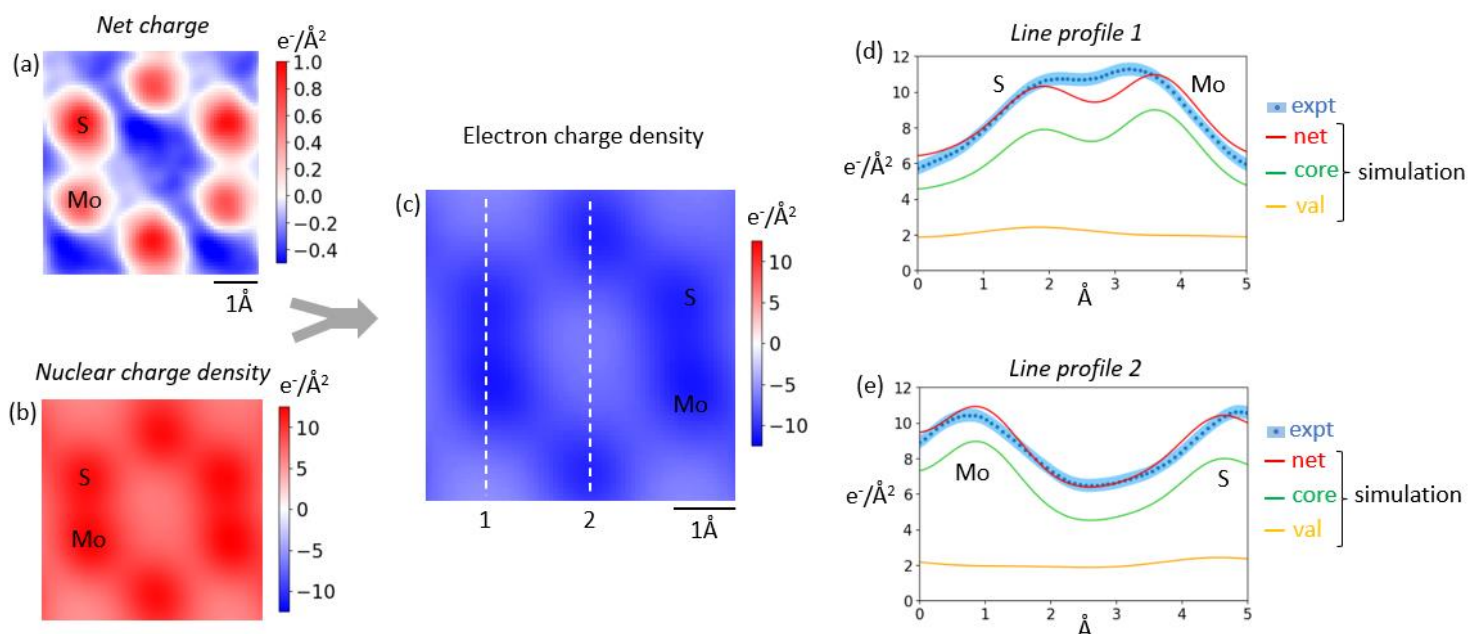


Figure 5 | Deriving the electron charge density from experimental data. (a) Experimental electron charge density (b) Reconstructed nuclear charge density with probe convolution (c) Experimental electron charge density derived by subtracting (b) from (a); (d & e) Line profiles (1 & 2) for the experimental electron charge density and simulated charge density from Fig 4, showing the contributions of valence and core electrons to the overall electron charge density. The blue shaded region indicates two standard deviations on either side of the mean.

Supplementary Note 1

The ADF-STEM image was used to derive the nuclear charge image as shown in Figure S7.

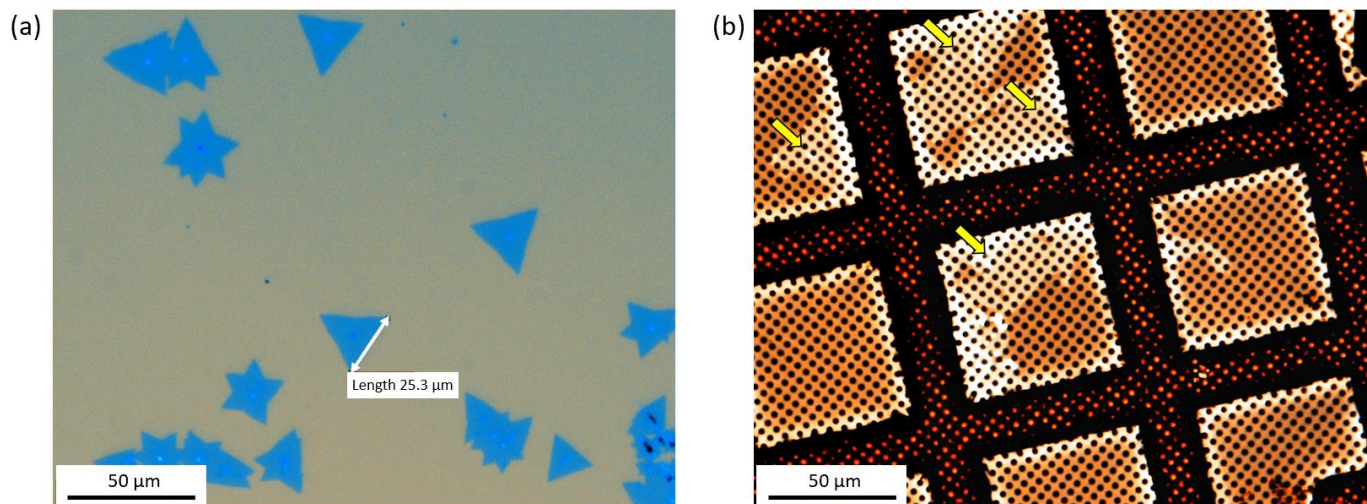
First, we used AtomSegNet to identify nuclear positions in the ADF image. Next, we determined the peak intensity of each atom in the ADF image using multimodal Gaussian fitting with in-house python code (the ADF image was normalized to the 0-1 range prior to Gaussian fitting).

The peak intensities obtained were:

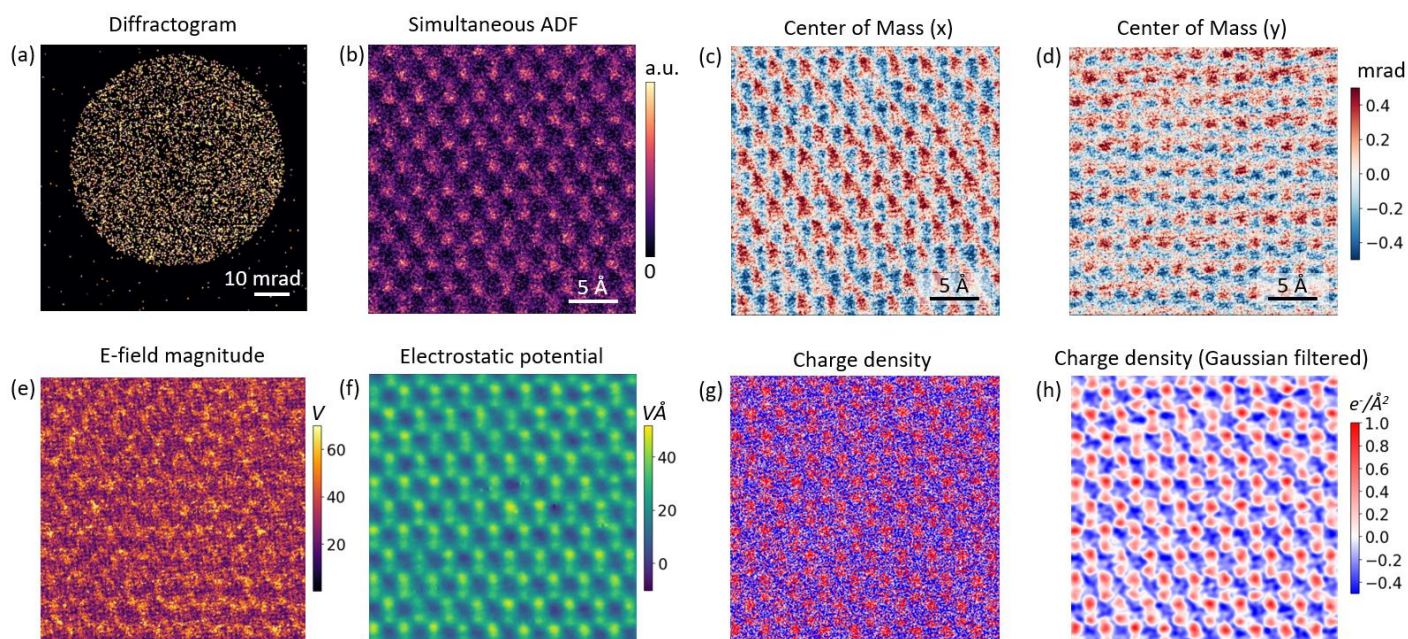
Mo atoms: 0.86, 0.73, 0.80 ; Average 0.8

S atoms: 0.46, 0.41, 0.54 ; Average 0.48

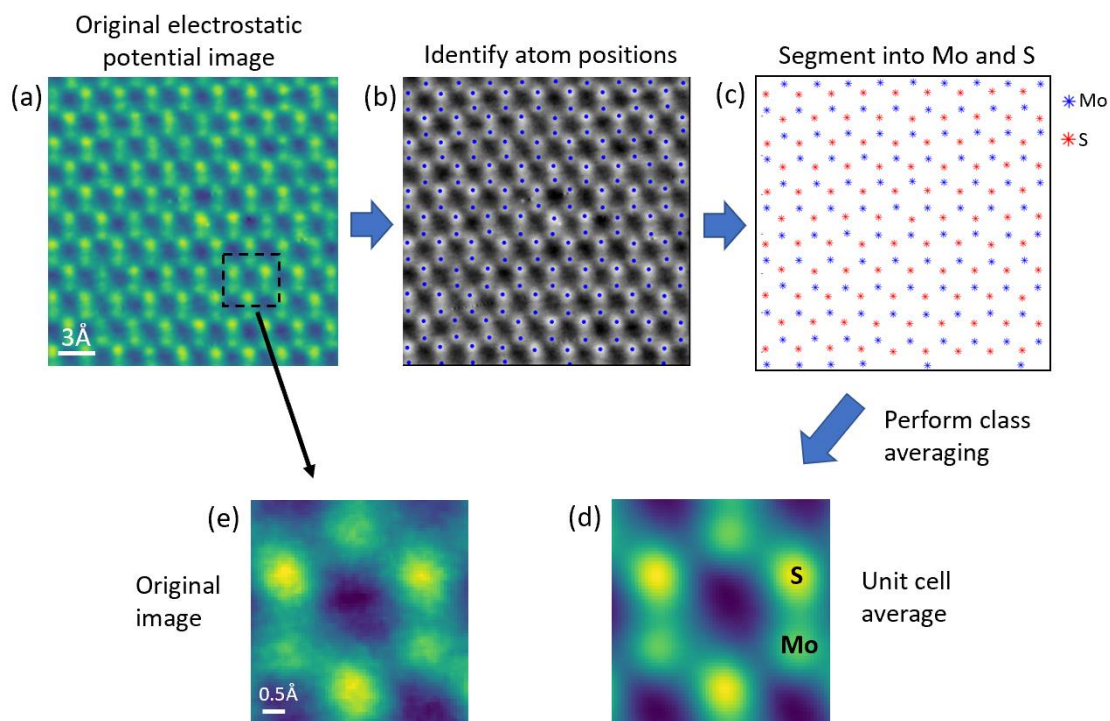
This gave us an peak intensity ratio of 1.67, corresponding to $Z^{1.9}$, where Z is the atomic number. We then assigned nuclear charges (42e⁻ for Mo and 16e⁻ for S) as delta functions at each atomic site. Finally, this was convolved with the probe intensity and a 1.1 Å FWHM Gaussian to obtain the nuclear charge density image.



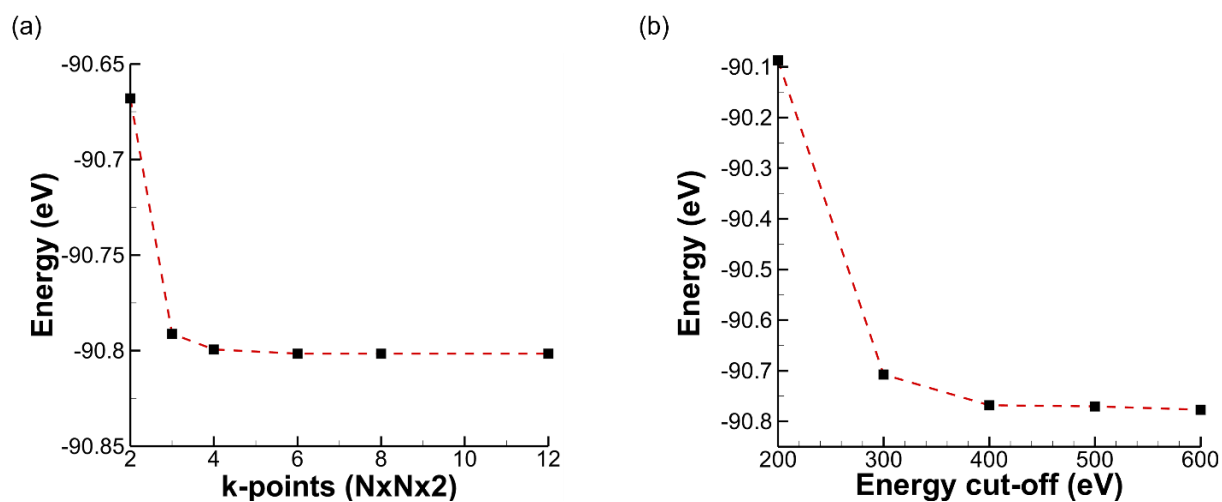
Supplementary Figure 1 | Optical images of MoS₂ flakes (a) Optical image of MoS₂ monolayer flakes on a SiO₂(285nm)/Si substrate (b) after transferring to a holey carbon TEM grid (yellow arrows indicate MoS₂ flakes).



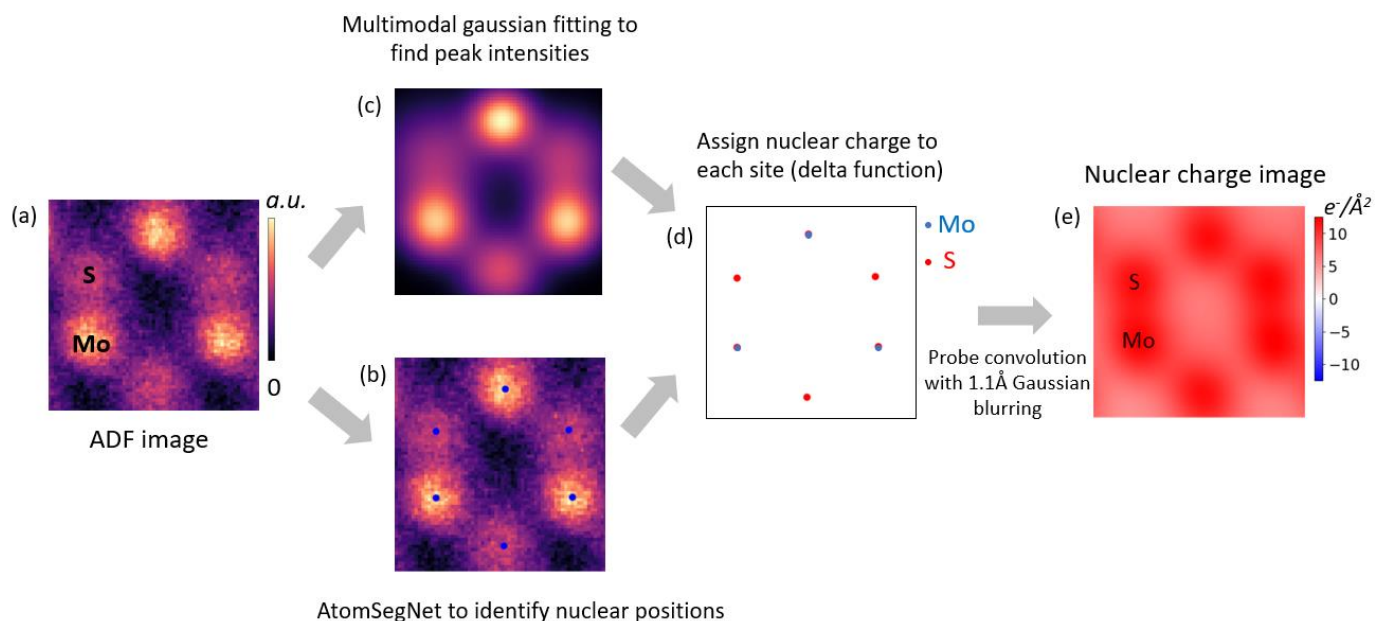
Supplementary Figure 2 | 4D STEM CoM dataset. (a) Typical diffractogram acquired at one probe position where each bright spot indicates a single electron detected by the camera (b) Simultaneously acquired ADF-STEM image with an annular detector (c) & (d) CoM images corresponding to probe positions in (b), calculated from diffractograms at each probe position (e) Electric field magnitude calculated from the CoM images (f) Electrostatic (projected) potential (g) charge density and (h) (g) after Gaussian blurring to reduce high frequency noise.



Supplementary Figure 3 | Unit cell averaging to improve SNR. (a) Original electrostatic potential image (b) (a) in greyscale with atom positions identified using AtomSegNet (c) Atoms segmented into Mo and S (d) Unit cell (class) averaged image compared with (e) the original image.



Supplementary Figure 4 | Convergence of DFT simulation. (a) The energy change with the number of k-points. (b) The energy change with the cut-off energy. A k-point grid of $8 \times 8 \times 2$ and a cut-off energy of 500 eV are chosen to ensure proper convergence of the simulations and have good computational efficiency.



Supplementary Figure 5 | Determining the nuclear charge density image. (a) Unit cell averaged ADF-STEM image, (b) Nuclear positions in (a) identified using AtomSegNet, (c) Multimodal Gaussian fit to (a), (d) Nuclear charges depicted as delta functions, (e) (d) convolved with the probe intensity along with source size blurring.